

3D-to-2D Transition of Anion Mobility in CsPbBr₃ under Pressure

Thijs J. A. M. Smolders, Alison B. Walker, and Matthew J. Wolf*

Department of Physics, University of Bath, Claverton Down, Bath, BA2 7AY, United Kingdom

E-mail: m.j.wolf@bath.ac.uk

Abstract

We study the effects of hydrostatic pressure in the range 0.0–2.0 GPa on anion mobility in the orthorhombic $Pnma$ phase of CsPbBr₃. Using density functional theory and the climbing nudged elastic band method, we calculate the transition states and activation energies for anions to migrate both within and between neighbouring PbBr₃ octahedra. The results of those calculations are used as input to a kinetic model for anion migration, which we solve in the steady state to determine the anion mobility tensor as a function of applied pressure. We find that the response of the mobility tensor to increasing pressure is highly anisotropic, being strongly enhanced in the (010) lattice plane and strongly reduced in the direction normal to it at elevated pressure. These results demonstrate the potentially significant influence of pressure and strain on the magnitude and direction of anion migration in lead–halide perovskites.

Over the past decade, lead–halide perovskites (LHPs) have emerged as promising materials for optoelectronic applications, most notably as active layers in photovoltaic cells^{1,2} and LEDs.^{3–5} One of the advantageous qualities of LHPs is that their properties may be readily tuned, which has most notably been achieved by altering the composition.^{6–9} More recently,

strain engineering has been suggested as an additional means of modifying the properties of LHPs.^{10,11} Residual levels of strain, resulting from lattice mismatch and thermal expansion mismatch, are known to strongly affect LHP properties.¹² In particular, enabled by the softness of the materials,^{13–16} pressure offers a particularly powerful way of inducing strain.^{17–20} The effects of pressure on the electronic properties of LHPs have been the subject of a number of experimental studies,^{21–23} and theoretical calculations have provided explanations for the observed behaviour in terms of the different modes of distortion of the lattice under pressure, and their effects on inter-ionic bond lengths and bond angles.^{24–29}

In addition to electronic transport, LHPs are also well known to exhibit significant ionic conductivity^{30–33} even at moderate temperatures, and moreover, ion transport has been implicated in a number of critical aspects of device performance, such as current–voltage hysteresis^{34,35} and the long-term stability^{32,33,36–38} of LHP-based devices. Furthermore, a number of recent studies have indicated that ionic conductivity in LHPs is also significantly affected by various manifestations of strain, both residual^{39,40} and pressure-induced.^{41–43} However, unlike the electrical conductivity, a detailed atomistic understanding of the influence of pressure on ion motion is currently lacking.

In this work, we carry out a quantitative analysis of the effects of pressure on ionic conductivity in the all-inorganic LHP CsPbBr₃. We compute migration barriers using density functional theory (DFT) and the climbing nudged elastic band method,^{44,45} and use the resulting activation energies as parameters in a kinetic scheme^{46,47} that we solve in the steady state to obtain a macroscopic anion mobility tensor as a function of applied pressure. CsPbBr₃ is a promising material for a number of applications, such as LEDs and photodetectors,^{48–50} although its band gap is generally considered to be too wide for applications in single junction solar cells. It adopts the same orthorhombic *Pnma* structure at low temperatures as other technologically relevant LHPs, such as MAPbI₃, MAPbBr₃ and FAPbBr₃,^{51–53} however, unlike those materials, it does not undergo a phase transition until well above room temperature.^{54,55} It is important to note that density functional theory (DFT) total energy

calculations effectively correspond to a temperature of 0 K, at which the commonly considered higher symmetry phases, such as the tetragonal $P4/mbm$ and cubic $Pm\bar{3}m$ phases, are unstable;^{56–58} additionally, several studies have suggested that these higher symmetry phases, which are typically observed at higher temperatures in halide perovskites, are in fact dynamical averages of the orthorhombic $Pnma$ phase,^{59–61} making CsPbBr_3 a good model system for the general class of LHPs.

Anion vacancies are believed to be the most mobile species in LHPs in general,^{62–69} and the positive charge state of the bromide vacancy in CsPbBr_3 has been shown to be the most stable one for Fermi levels within the majority of the band gap;^{70–73} therefore, we restrict our study to the migration of positively charged bromide vacancies.

Perovskite structures of stoichiometry ABX_3 are formed of corner sharing octahedra of X anions, with B cations at their centres and A cations in the voids between them. The perovskite structure of highest symmetry, the so-called “aristotype”, is a cubic structure of space group $Pm\bar{3}m$, with a unit cell that contains a single ABX_3 formula unit. Lower symmetry perovskite structures are thought of primarily as resulting from taking the aristotype and tilting neighbouring octahedra with respect to one another. In the orthorhombic $Pnma$ structure, the tilting pattern corresponds to in-phase tilts about the long (**b**) lattice vector, and out-of-phase tilts along the other two lattice vectors ($a^-b^+a^-$ in the notation of Glazer⁷⁴), resulting in a unit cell which contains four ABX_3 formula units.

The lower symmetry of the orthorhombic structure with respect to the cubic one has important implications for the number of elementary anion migration paths connecting pairs of lattice sites that must be considered.⁷⁵ Firstly, while all anion sites are symmetrically equivalent in the cubic structure, in the orthorhombic structure there are two symmetrically inequivalent sites, corresponding to the 4c and 8d Wyckoff positions, which we describe as being either apical or equatorial respectively, and which are shown in Figure 1 as either pink or black spheres, respectively. Thus, each migration event proceeds from one of two types of site. Secondly, while each of the eight first-nearest neighbours (1-NNs) of a given halide

site, which correspond to the final site of a migration event, are symmetrically equivalent (with respect to the point group of the site) in the cubic structure, this is not the case in the orthorhombic structure, as we will now discuss in more detail.

We first consider the point group symmetry at the apical site. All of its 1-NN bromide sites are of the equatorial type, and belong to the two octahedra that are corner-sharing through the apical bromide. By virtue of the mirror symmetry at the apical site, these octahedra are symmetrically equivalent, and therefore, the eight 1-NNs can be grouped into four symmetrically inequivalent pairs. Next, we look at the local symmetry at the equatorial position. Of its eight 1-NNs, four are apical and the relation between them has already been discussed above. This leaves four remaining 1-NNs, all of which are equatorial, and a screw symmetry axis reduces the remaining four neighbours to two symmetrically inequivalent pairs. A visual representation of the resulting six symmetrically inequivalent pairs of initial and final bromide sites involved in elementary migration events is shown in Figure 1.

To find the migration paths and activation energies for each of the elementary migration events (defined by the symmetrically inequivalent pairs of initial and final bromide lattice sites), climbing nudged elastic band (CNEB) calculations, based on density functional theory, were carried out. The results of the calculations are shown in Figure 1. Relative to the aristotype, the reduced symmetry of the *Pnma* structure results in a significant spread in barrier heights for the different transitions. The magnitudes, in the range of 0.23–0.34 eV, are in line with values reported in experimental studies^{76,77} and theoretical calculations of ion migration in the higher symmetry tetragonal and cubic phases.^{43,65}

Any long range migration of vacancies requires multiple hops along symmetrically inequivalent elementary paths, so that the individual barriers are insufficient to draw meaningful quantitative conclusions; in particular, the connectivity of the lattice must be taken into account. In order to do so, we set up a kinetic scheme, described in detail in the computational methods, in which we account for the full connectivity of the lattice, and parametrise it using the activation barriers computed using DFT. We then use the kinetic

scheme to compute the macroscopic mobility tensor $\boldsymbol{\mu}$, defined by the following equation:

$$\vec{v}_d = \boldsymbol{\mu} \vec{E} \tag{1}$$

The eigenvectors of $\boldsymbol{\mu}$ are parallel to the lattice vectors, and the corresponding eigenvalues at 300 K (and 0.0 GPa) are 2.2, 4.8, $3.5 \times 10^{-6} \text{ cm}^2\text{V}^{-1}\text{s}^{-1}$ in the [100], [010] and [001] directions respectively. A decomposition of the elements into contributions from each of the symmetrically inequivalent paths, shown in the bottom right of Figure 1, indicates that multiple paths contribute to the mobility in each of the principal directions, leading to an essentially isotropic mobility; in contrast, taking any *one* of the computed migration barriers, and calculating the mobility at 300K simply via the Arrhenius equation and Einstein relation, leads to values for the mobility which vary by two orders of magnitude, emphasising the importance of taking the full connectivity of the lattice into account.

We then start applying hydrostatic pressure, in the range of 0.0–2.0 GPa, to the *Pnma* unit cell while constraining the space group, which is consistent with the experimentally and computationally observed stability range.^{24,25,27,78,79} Despite the pressure being isotropic, the structural response is significantly anisotropic, such that the length of **c** is reduced to about 90% of its unstrained value at 2.0 GPa, in agreement with previous work.⁷⁸ In contrast, the lengths of **a** and **b** remain largely unaltered, rising and falling, respectively, by approximately 1%.

In addition to the change in lattice vectors, the internal co-ordinates of the ions respond strongly to the applied pressure. This is mainly apparent in the equatorial (010) plane, where the octahedra exhibit enhanced tilting, leading to a structure described in previous publications as a “squeezed wine-rack”,⁷⁸ as also observed in Refs.^{24,25,27,79} As a result, there is a significant reduction in the distances between Br sites in neighbouring octahedra. One second-nearest-neighbour distance in particular, shown in Figure 2, is significantly reduced under pressure, such that it approaches the range of values of 1-NN distances. Therefore, we also compute the activation energy for migration between that 2-NN pair of ions under

pressure.

The evolution under pressure of the activation energies for migration between all seven pairs of sites under consideration is shown in Figure 2. While most migration barriers increase with pressure, the barriers corresponding to two E-to-E transitions, including the 2-NN path discussed above, decrease such that they are significantly lower at 2.0 GPa, with values of 0.17 eV.

The lowering of the energy barriers corresponding to the two paths has significant implications for the mobility at higher pressures, as the solution of the kinetic scheme shows. For all pressures, the eigenvectors of the mobility tensor remain along the crystalline [100], [010] and [001] directions; however, as shown in the left of Figure 3, the relative magnitudes of their eigenvalues change dramatically with increasing pressure such that at 2.0 GPa, the mobility in the equatorial (010) plane is approximately 3 orders of magnitude higher than in the direction normal to it (parallel to [010]), leading to an effective 3D-to-2D transition in the mobility. A decomposition of the diagonal components of the mobility tensor in terms of the contributions of symmetrically inequivalent transitions shows that migration at 2.0 GPa is predominantly due to two transitions, namely the cyan and the magenta transitions shown in Figure 3, for which the migration barriers decrease significantly at elevated pressures.

Due to the significant anisotropy of the mobility at elevated pressures, ion migration can either be strongly enhanced or strongly reduced depending on the orientation of the crystal with respect to the applied electric field. This effect could be exploited to control ion migration in layered devices, for example, where the lattice vectors and thermal coefficient of the LHP typically differ from that of the substrate. As a result, an intrinsic level of strain will be present at the interface between the perovskite film and the substrate, directly affecting the ionic migration in the vicinity of the interfaces even without using external pressure.

Finally, we note that the elastic constants of MAPbI₃, MAPbBr₃ and CsPbI₃ in the *Pnma* phase show similar behaviour to CsPbBr₃, with c_{22} being significantly higher than

c_{11} and c_{33} .¹⁵ As such, a similar anisotropic structural response to applied pressure might be expected, though this possibility, and its effects on ion migration, needs to be investigated further, particularly in light of the differences in bonding due to the organic molecule in the hybrid LHPs, and possible phase transitions under pressure.

In conclusion, we have studied the effects of pressure on anion migration barriers and mobility, using a combination of DFT calculations and kinetic modelling. Our results demonstrate that a proper consideration of the point group symmetry and connectivity of the lattice structure of CsPbBr_3 is necessary to model and understand anionic migration. At low pressures, anion migration proceeds via sequential transitions between multiple first-nearest neighbour (1-NN) pairs of sites, and is essentially isotropic. As pressure is increased, most of the barriers associated with transitions between 1-NN pairs increase, with only one decreasing significantly. Additionally, the activation energy for a transition between 2-NN halide sites is lowered significantly at higher pressures. The two effects combined lead to significantly enhanced mobilities in the equatorial plane, and a significantly reduced mobility normal to it, corresponding to an effective transition from 3D mobility in the absence of pressure, to effective 2D mobility at 2.0 GPa. This points to the potential of strain engineering perovskites to control the level of ionic migration in LHPs, in addition to their electronic properties.

Methods: Density functional theory calculations

Our DFT calculations were performed using the SCAN (strongly constrained and appropriately normed) meta-GGA exchange–correlation functional⁸⁰ and the PAW method for treating the effects of the atomic cores on the valence electrons,⁸¹ as implemented in the Vienna *ab initio* simulation package (VASP) code, version 5.4.4.⁸² We use the SCAN functional as it has been shown to outperform other exchange–correlation functionals in terms of the lattice parameters of perovskites,⁸³ the local potential energy surface,⁸⁴ the pressure-induced phase transitions⁸⁵ and lattice formation enthalpy.⁸⁶

Optimisation of both the lattice parameters and the atomic coordinates was performed on

the orthorhombic unit cell of CsPbBr₃, containing four formula units, under the constraint that the *Pnma* space group of the structure was preserved, until both the energy change and change of eigenvalues between two self-consistent cycles were below 10⁻⁸ eV and the residual forces were below 0.001 eV Å⁻¹. The plane-wave cut-off energy was set to 600 eV. An 8 × 6 × 8 Γ -centred *k*-point mesh was used, generated automatically according to the Monkhorst–Pack scheme.⁸⁷

The calculations involving bromide vacancies were performed in a supercell of the orthorhombic phase, which was generated by using a [[2,0,2],[0,2,0],[-2,0,2]] scaling matrix on the *Pnma* unit cell, and contains 320 atoms/64 formula units of the pristine lattice. Positively charged bromide vacancies were introduced in the cell, and, while keeping the lattice parameters fixed, internal coordinates were optimised using a plane-wave cutoff energy of 300 eV, evaluated at the Γ -point only, until both the energy change and change of eigenvalues between two self-consistent were below 10⁻⁶ eV and the residual forces were below 0.01 eV Å⁻¹.

To determine the ion migration paths and the associated activation energies, climbing nudged elastic band (CNEB) calculations were performed as implemented in the VASP Transition State Tools (VTST) package.^{44,45} The migration path was evaluated using four structural images, with a spring constant of 5 eV/Å² connecting the images. Internal coordinates were optimised using a plane-wave cutoff energy of 300 eV, evaluated at the Γ -point only, until both the energy change and change of eigenvalues between two self-consistent were below 10⁻⁶ eV and the residual forces were below 0.05 eV Å⁻¹.

Methods: Kinetic scheme and mobility tensor calculations

To calculate the mobility tensor, we set up the kinetic scheme as a Continuous-Time Markov Chain, and consider a set of states of the system, each of which corresponds to a vacancy occupying a site in the unit cell.^{46,47} The variables in the scheme are the probabilities of each state being occupied, the time dependence of which is given by solutions to a master equation:

$$\frac{d\vec{P}}{dt} = \mathbf{Q}\vec{P}. \quad (2)$$

In Equation 2, the elements of \vec{P} , P_j , are the probabilities of a vacancy occupying sites j at time t , and the elements of the *transition rate matrix* \mathbf{Q} , Q_{ij} , are the rates (probabilities per unit time) for a vacancy to hop from site j to site i . The transition rates, which are time independent in our scheme, are calculated using the Arrhenius expression:

$$Q_{ij} = A \exp(-\beta(E_a)_{ij}), \quad (3)$$

in which $\beta = (k_B T)^{-1}$, $(E_a)_{ij}$ is the activation energy for a vacancy to hop from site j to site i , and A is the attempt frequency for the process to take place, which we assume to be the same for all pairs i and j . In our calculations, we assume a temperature T of 300 K and an attempt frequency ν of $2 \times 10^{12} \text{ s}^{-1}$, which we approximate based on the Raman frequency of 70 cm^{-1} corresponding to the inorganic PbBr_6 cage,^{78,88} and which we assume is constant with pressure,⁷⁸ in accordance with earlier work on LHPs.⁴³ $(E_a)_{ij}$ is taken as the sum of the result of the DFT CNEB calculation described above, which we denote $(E_a^0)_{ij}$, and a field dependent part, which we calculate simply as the difference in potential energy between site j and the location of the moving anion at the (energetic) saddle point of its path between sites i and j (which corresponds to the hopping of the vacancy between sites j and i):

$$(E_a)_{ij} = (E_a^0)_{ij} + q(\vec{r}_{\text{saddle}} - \vec{r}_j) \cdot \vec{E}$$

where we use the formal charge q of -1.0 for the moving anion.⁸⁹ We note that this approach is a generalisation of the approach adopted originally by Mott and Gurney.⁹⁰⁻⁹² Further, we stress that the internal electric field \vec{E}_{int} will differ from the applied field \vec{E} and will depend strongly on the experimental conditions, as such we do not account for it in our model.

In order to compute the mobility, we “apply” a finite electric field, and then solve Equation 2 in the steady state:

$$\frac{d\vec{P}}{dt} = \vec{0} = \mathbf{Q}\vec{P}. \quad (4)$$

We can do so by finding the eigenvectors of the rate matrix, with the one with eigenvalue 0 corresponding to steady state. We note that at equilibrium (i.e. zero field), they would have values given by Boltzmann factors of the vacancy formation energy, but when a field is applied that is no longer the case.

Once we have the steady state probabilities P_j , we can compute the flux from state j into i —that is, the number of hopping events of a vacancy between those sites, per unit time—is $Q_{ij}P_j$, and finally the drift velocity \vec{v}_d as the sum of the fluxes multiplied by the displacement vectors associated with each hop, $\vec{r}_i - \vec{r}_j$:

$$\vec{v}_d = \sum_j \sum_{i \neq j} Q_{ij} P_j (\vec{r}_i - \vec{r}_j) \quad (5)$$

To obtain the components of the full mobility tensor μ , we apply a field along the crystalline axes [100], [010] and [001] in turn, and then compute \vec{v}_d by summing over all hops. In general, one can diagonalise the tensor matrix, in order to obtain the mobility eigenvalues and the corresponding directions. In our study, we find that the eigenvectors of the mobility tensor are parallel to the lattice vectors.

Acknowledgement

We acknowledge funding from the European Union’s Horizon 2020 MSCA Innovative Train-

ing Network under grant agreement number 764787, and the Energy Oriented Centre of Excellence (EoCoE-II), grant agreement number 676629. This research made use of the Balena High Performance Computing (HPC) Service at the University of Bath; and the Isambard UK National Tier-2 HPC Service (<http://gw4.ac.uk/isambard/>) operated by GW4 and the UK Meteorological Office, and funded by EPSRC (EP/P020224/1). We thank Drs. I. R. Thompson and W. R. Saunders for discussions pertaining to kinetic modelling, and Dr. T. Duchoň for commenting on the manuscript.

References

- (1) Snaith, H. J. Present status and future prospects of perovskite photovoltaics. *Nature Materials* **2018**, *17*, 372–376.
- (2) Jena, A. K.; Kulkarni, A.; Miyasaka, T. Halide Perovskite Photovoltaics: Background, Status, and Future Prospects. *Chemical Reviews* **2019**, *119*, 3036–3103.
- (3) Service, R. F. Perovskite LEDs begin to shine. *Science* **2019**, *364*, 918.
- (4) Lu, M.; Zhang, Y.; Wang, S.; Guo, J.; Yu, W. W.; Rogach, A. L. Metal Halide Perovskite Light-Emitting Devices: Promising Technology for Next-Generation Displays. *Advanced Functional Materials* **2019**, *29*, 1–35.
- (5) Liu, X. K.; Xu, W.; Bai, S.; Jin, Y.; Wang, J.; Friend, R. H.; Gao, F. Metal halide perovskites for light-emitting diodes. *Nature Materials* **2020**, *20*.
- (6) Protesescu, L.; Yakunin, S.; Bodnarchuk, M. I.; Krieg, F.; Caputo, R.; Hendon, C. H.; Yang, R. X.; Walsh, A.; Kovalenko, M. V. Nanocrystals of Cesium Lead Halide Perovskites (CsPbX₃, X = Cl, Br, and I): Novel Optoelectronic Materials Showing Bright Emission with Wide Color Gamut. *Nano Letters* **2015**, *15*, 3692–3696.

- (7) Jeon, N. J.; Noh, J. H.; Yang, W. S.; Kim, Y. C.; Ryu, S.; Seo, J.; Seok, S. I. Compositional engineering of perovskite materials for high-performance solar cells. *Nature* **2015**, *517*, 476–480.
- (8) Saliba, M.; Matsui, T.; Seo, J. Y.; Domanski, K.; Correa-Baena, J. P.; Nazeeruddin, M. K.; Zakeeruddin, S. M.; Tress, W.; Abate, A.; Hagfeldt, A.; Grätzel, M. Cesium-containing triple cation perovskite solar cells: Improved stability, reproducibility and high efficiency. *Energy and Environmental Science* **2016**, *9*, 1989–1997.
- (9) Li, J.; Wang, Q.; Abate, A. Perovskite solar cells. *Nanomaterials for Solar Cell Applications* **2019**, 417–446.
- (10) Zhu, C. et al. Strain engineering in perovskite solar cells and its impacts on carrier dynamics. *Nature Communications* **2019**, *10*.
- (11) Kim, H. S.; Park, N. G. Importance of tailoring lattice strain in halide perovskite crystals. *NPG Asia Materials* **2020**, *12*.
- (12) Jones, T. W. et al. Lattice strain causes non-radiative losses in halide perovskites. *Energy and Environmental Science* **2019**, *12*, 596–606.
- (13) Sun, S.; Fang, Y.; Kieslich, G.; White, T. J.; Cheetham, A. K. Mechanical properties of organic-inorganic halide perovskites, $\text{CH}_3\text{NH}_3\text{PbX}_3$ ($X = \text{I}, \text{Br}$ and Cl), by nanoindentation. *Journal of Materials Chemistry A* **2015**, *3*, 18450–18455.
- (14) Létoublon, A.; Paofai, S.; Rufflé, B.; Bourges, P.; Hehlen, B.; Michel, T.; Ecolivet, C.; Durand, O.; Cordier, S.; Katan, C.; Even, J. Elastic Constants, Optical Phonons, and Molecular Relaxations in the High Temperature Plastic Phase of the $\text{CH}_3\text{NH}_3\text{PbBr}_3$ Hybrid Perovskite. *Journal of Physical Chemistry Letters* **2016**, *7*, 3776–3784.
- (15) Lee, J. H.; Deng, Z.; Bristowe, N. C.; Bristowe, P. D.; Cheetham, A. K. The competition between mechanical stability and charge carrier mobility in MA-based hybrid

- perovskites: insight from DFT. *Journal of Materials Chemistry C* **2018**, *6*, 12252–12259.
- (16) Ferreira, A. C.; Létoublon, A.; Paofai, S.; Raymond, S.; Ecolivet, C.; Rufflé, B.; Cordier, S.; Katan, C.; Saidaminov, M. I.; Zhumekenov, A. A.; Bakr, O. M.; Even, J.; Bourges, P. Elastic Softness of Hybrid Lead Halide Perovskites. *Physical Review Letters* **2018**, *121*, 1–6.
- (17) Jaffe, A.; Lin, Y.; Karunadasa, H. I. Halide Perovskites under Pressure: Accessing New Properties through Lattice Compression. *ACS Energy Letters* **2017**, *2*, 1549–1555.
- (18) Li, Q.; Zhang, L.; Chen, Z.; Quan, Z. Metal halide perovskites under compression. *Journal of Materials Chemistry A* **2019**, *7*, 16089–16108.
- (19) Liu, G.; Kong, L.; Yang, W.; Mao, H.-k. Pressure engineering of photovoltaic perovskites. *Materials Today* **2019**, *27*, 91–106.
- (20) Jiao, Y.; Yi, S.; Wang, H.; Li, B.; Hao, W.; Pan, L.; Shi, Y.; Li, X.; Liu, P.; Zhang, H.; Gao, C.; Zhao, J.; Lu, J. Strain Engineering of Metal Halide Perovskites on Coupling Anisotropic Behaviors. *Advanced Functional Materials* **2020**, *2006243*, 1–22.
- (21) Jaffe, A.; Lin, Y.; Karunadasa, H. I. Halide Perovskites under Pressure: Accessing New Properties through Lattice Compression. *ACS Energy Letters* **2017**, *2*, 1549–1555.
- (22) Lü, X.; Yang, W.; Jia, Q.; Xu, H. Pressure-induced dramatic changes in organic-inorganic halide perovskites. *Chemical Science* **2017**, *8*, 6764–6776.
- (23) Li, M.; Liu, T.; Wang, Y.; Yang, W.; Lü, X. Pressure responses of halide perovskites with various compositions, dimensionalities, and morphologies. *Matter and Radiation at Extremes* **2020**, *5*.
- (24) Xiao, G.; Cao, Y.; Qi, G.; Wang, L.; Liu, C.; Ma, Z.; Yang, X.; Sui, Y.; Zheng, W.; Zou, B. Pressure Effects on Structure and Optical Properties in Cesium Lead Bromide

- Perovskite Nanocrystals. *Journal of the American Chemical Society* **2017**, *139*, 10087–10094.
- (25) Huang, Y.; Wang, L.; Ma, Z.; Wang, F. Pressure-Induced Band Structure Evolution of Halide Perovskites: A First-Principles Atomic and Electronic Structure Study. *Journal of Physical Chemistry C* **2019**, *123*, 739–745.
- (26) Wang, F.; Tan, M.; Li, C.; Niu, C.; Zhao, X. Unusual pressure-induced electronic structure evolution in organometal halide perovskite predicted from first-principles. *Organic Electronics* **2019**, *67*, 89–94.
- (27) Wang, Y.; Long, R. Unravelling the Effects of Pressure-Induced Suppressed Electron-Hole Recombination in CsPbBr₃ Perovskite: Time-Domain ab Initio Analysis. *Journal of Physical Chemistry Letters* **2019**, *10*, 4354–4361.
- (28) Ghosh, D.; Aziz, A.; Dawson, J. A.; Walker, A. B.; Islam, M. S. Putting the Squeeze on Lead Iodide Perovskites: Pressure-Induced Effects to Tune Their Structural and Optoelectronic Behavior. *Chemistry of Materials* **2019**, *31*, 4063–4071.
- (29) Li, W.; Chen, Z.; Tang, J.; Prezhdov, O. V. Anti-correlation between Band gap and Carrier Lifetime in Lead Halide Perovskites under Compression Rationalized by Ab Initio Quantum Dynamics. *Chemistry of Materials* **2020**, *32*, 4707–4715.
- (30) Pockett, A.; Eperon, G. E.; Sakai, N.; Snaith, H. J.; Peter, L. M.; Cameron, P. J. Microseconds, milliseconds and seconds: Deconvoluting the dynamic behaviour of planar perovskite solar cells. *Physical Chemistry Chemical Physics* **2017**, *19*, 5959–5970.
- (31) Tress, W. Metal Halide Perovskites as Mixed Electronic-Ionic Conductors: Challenges and Opportunities - From Hysteresis to Memristivity. *Journal of Physical Chemistry Letters* **2017**, *8*, 3106–3114.

- (32) Walsh, A.; Stranks, S. D. Taking Control of Ion Transport in Halide Perovskite Solar Cells. *ACS Energy Letters* **2018**, *3*, 1983–1990.
- (33) Lee, J. W.; Kim, S. G.; Yang, J. M.; Yang, Y.; Park, N. G. Verification and mitigation of ion migration in perovskite solar cells. *APL Materials* **2019**, *7*.
- (34) Richardson, G.; O’Kane, S. E.; Niemann, R. G.; Peltola, T. A.; Foster, J. M.; Cameron, P. J.; Walker, A. B. Can slow-moving ions explain hysteresis in the current-voltage curves of perovskite solar cells? *Energy and Environmental Science* **2016**, *9*, 1476–1485.
- (35) Habisreutinger, S. N.; Noel, N. K.; Snaith, H. J. Hysteresis Index: A Figure without Merit for Quantifying Hysteresis in Perovskite Solar Cells. *ACS Energy Letters* **2018**, 2472–2476.
- (36) Yuan, Y.; Huang, J. Ion Migration in Organometal Trihalide Perovskite and Its Impact on Photovoltaic Efficiency and Stability. *Accounts of Chemical Research* **2016**, *49*, 286–293.
- (37) Zhang, T.; Hu, C.; Yang, S. Ion Migration: A “Double-Edged Sword” for Halide-Perovskite-Based Electronic Devices. 2020.
- (38) Zhao, Y.; Zhou, W.; Han, Z.; Yu, D.; Zhao, Q. Effects of ion migration and improvement strategies for the operational stability of perovskite solar cells. *Physical Chemistry Chemical Physics* **2021**, *23*, 94–106.
- (39) Zhao, J.; Deng, Y.; Wei, H.; Zheng, X.; Yu, Z.; Shao, Y.; Shield, J. E.; Huang, J. Strained hybrid perovskite thin films and their impact on the intrinsic stability of perovskite solar cells. *Science Advances* **2017**, *3*.
- (40) Xue, D. J.; Hou, Y.; Liu, S. C.; Wei, M.; Chen, B.; Huang, Z.; Li, Z.; Sun, B.; Proppe, A. H.; Dong, Y.; Saidaminov, M. I.; Kelley, S. O.; Hu, J. S.; Sargent, E. H.

- Regulating strain in perovskite thin films through charge-transport layers. *Nature Communications* **2020**, *11*.
- (41) Ou, T.; Ma, X.; Yan, H.; Shen, W.; Liu, H.; Han, Y.; Liu, X.; Liu, C.; Ma, Y.; Gao, C. Pressure effects on the inductive loop, mixed conduction, and photoresponsivity in formamidinium lead bromide perovskite. *Applied Physics Letters* **2018**, *113*, 6–11.
- (42) Ou, T.; Liu, C.; Yan, H.; Han, Y.; Wang, Q.; Liu, X.; Ma, Y.; Gao, C. Effects of pressure on the ionic transport and photoelectrical properties of CsPbBr₃. *Applied Physics Letters* **2019**, *114*, 062105.
- (43) Muscarella, L. A.; Hutter, E. M.; Wittmann, F.; Woo, Y. W.; Jung, Y.-K.; McGovern, L.; Versluis, J.; Walsh, A.; Bakker, H. J.; Ehrler, B. Lattice Compression Increases the Activation Barrier for Phase Segregation in Mixed-Halide Perovskites. *ACS Energy Letters* **2020**, 3152–3158.
- (44) Henkelman, G.; Uberuaga, B. P.; Jónsson, H. Climbing image nudged elastic band method for finding saddle points and minimum energy paths. *Journal of Chemical Physics* **2000**, *113*, 9901–9904.
- (45) Sheppard, D.; Terrell, R.; Henkelman, G. Optimization methods for finding minimum energy paths. *Journal of Chemical Physics* **2008**, *128*, 1–10.
- (46) Bányai, L.; Aldea, A. Master Equation Approach to the Hopping Transport Theory. *Fortschritte der Physik* **1979**, *27*, 435–462.
- (47) Allnatt, A.; Lidiard, A. *Atomic Transport of Solids*; Cambridge University Press, 2003; pp 216–246.
- (48) Kovalenko, M. V.; Protesescu, L.; Bodnarchuk, M. I. Properties and potential optoelectronic applications of lead halide perovskite nanocrystals. *Science* **2017**, *358*, 745–750.

- (49) Shen, K.; Xu, H.; Li, X.; Guo, J.; Sathasivam, S.; Wang, M.; Ren, A.; Choy, K. L.; Parkin, I. P.; Guo, Z.; Wu, J. Flexible and Self-Powered Photodetector Arrays Based on All-Inorganic CsPbBr₃ Quantum Dots. *Advanced Materials* **2020**, *32*.
- (50) Yu, J.; Liu, G.; Chen, C.; Li, Y.; Xu, M.; Wang, T.; Zhao, G.; Zhang, L. Perovskite CsPbBr₃ crystals: Growth and applications. *Journal of Materials Chemistry C* **2020**, *8*, 6326–6341.
- (51) Lee, J. H.; Bristowe, N. C.; Lee, J. H.; Lee, S. H.; Bristowe, P. D.; Cheetham, A. K.; Jang, H. M. Resolving the Physical Origin of Octahedral Tilting in Halide Perovskites. *Chemistry of Materials* **2016**, *28*, 4259–4266.
- (52) Bernasconi, A.; Malavasi, L. Direct evidence of permanent octahedra distortion in MAPbBr₃ hybrid perovskite. *ACS Energy Letters* **2017**, *2*, 863–868.
- (53) Schueller, E. C.; Laurita, G.; Fabini, D. H.; Stoumpos, C. C.; Kanatzidis, M. G.; Seshadri, R. Crystal Structure Evolution and Notable Thermal Expansion in Hybrid Perovskites Formamidinium Tin Iodide and Formamidinium Lead Bromide. *Inorganic Chemistry* **2018**, *57*, 695–701.
- (54) Stoumpos, C. C.; Malliakas, C. D.; Peters, J. A.; Liu, Z.; Sebastian, M.; Im, J.; Chasapis, T. C.; Wibowo, A. C.; Chung, D. Y.; Freeman, A. J.; Wessels, B. W.; Kanatzidis, M. G. Crystal growth of the perovskite semiconductor CsPbBr₃: A new material for high-energy radiation detection. *Crystal Growth and Design* **2013**, *13*, 2722–2727.
- (55) Malyshkin, D.; Sereda, V.; Ivanov, I.; Mazurin, M.; Sednev-Lugovets, A.; Tsvetkov, D.; Zuev, A. New phase transition in CsPbBr₃. *Materials Letters* **2020**, *278*.
- (56) Whalley, L. D.; Skelton, J. M.; Frost, J. M.; Walsh, A. Phonon anharmonicity, lifetimes, and thermal transport in CH₃NH₃PbI₃ from many-body perturbation theory. *Physical Review B* **2016**, *94*, 1–5.

- (57) Yang, R. X.; Skelton, J. M.; Da Silva, E. L.; Frost, J. M.; Walsh, A. Spontaneous octahedral tilting in the cubic inorganic cesium halide perovskites CsSnX₃ and CsPbX₃ (X = F, Cl, Br, I). *Journal of Physical Chemistry Letters* **2017**, *8*, 4720–4726.
- (58) Marronnier, A.; Lee, H.; Geffroy, B.; Even, J.; Bonnassieux, Y.; Roma, G. Structural Instabilities Related to Highly Anharmonic Phonons in Halide Perovskites. *Journal of Physical Chemistry Letters* **2017**, *8*, 2659–2665.
- (59) Bechtel, J. S.; Van Der Ven, A. Octahedral tilting instabilities in inorganic halide perovskites. *Physical Review Materials* **2018**, *2*, 1–13.
- (60) Klarbring, J. Low-energy paths for octahedral tilting in inorganic halide perovskites. *Physical Review B* **2019**, *99*, 1–7.
- (61) Bechtel, J. S.; Thomas, J. C.; Van Der Ven, A. Finite-temperature simulation of anharmonicity and octahedral tilting transitions in halide perovskites. *Physical Review Materials* **2019**, *3*, 1–10.
- (62) Eames, C.; Frost, J. M.; Barnes, P. R.; O’Regan, B. C.; Walsh, A.; Islam, M. S. Ionic transport in hybrid lead iodide perovskite solar cells. *Nature Communications* **2015**, *6*, 2–9.
- (63) Haruyama, J.; Sodeyama, K.; Han, L.; Tateyama, Y. First-principles study of ion diffusion in perovskite solar cell sensitizers. *Journal of the American Chemical Society* **2015**, *137*, 10048–10051.
- (64) Azpiroz, J. M.; Mosconi, E.; Bisquert, J.; De Angelis, F. Defect migration in methylammonium lead iodide and its role in perovskite solar cell operation. *Energy and Environmental Science* **2015**, *8*, 2118–2127.
- (65) Meloni, S.; Moehl, T.; Tress, W.; Franckeviius, M.; Saliba, M.; Lee, Y. H.; Gao, P.; Nazeeruddin, M. K.; Zakeeruddin, S. M.; Rothlisberger, U.; Graetzel, M. Ionic

- polarization-induced current-voltage hysteresis in CH₃NH₃PbX₃ perovskite solar cells. *Nature Communications* **2016**, *7*.
- (66) Mosconi, E.; De Angelis, F. Mobile Ions in Organohalide Perovskites: Interplay of Electronic Structure and Dynamics. *ACS Energy Letters* **2016**, *1*, 182–188.
- (67) Luo, Y.; Khoram, P.; Brittman, S.; Zhu, Z.; Lai, B.; Ong, S. P.; Garnett, E. C.; Fenning, D. P. Direct Observation of Halide Migration and its Effect on the Photoluminescence of Methylammonium Lead Bromide Perovskite Single Crystals. *Advanced Materials* **2017**, *29*, 1–7.
- (68) Chen, C.; Fu, Q.; Guo, P.; Chen, H.; Wang, M.; Luo, W.; Zheng, Z. Ionic transport characteristics of large-size CsPbBr₃ single crystals. *Materials Research Express* **2019**, *6*.
- (69) Zhang, B. B.; Wang, F.; Zhang, H.; Xiao, B.; Sun, Q.; Guo, J.; Hafsia, A. B.; Shao, A.; Xu, Y.; Zhou, J. Defect proliferation in CsPbBr₃ crystal induced by ion migration. *Applied Physics Letters* **2020**, *116*.
- (70) Shi, H.; Du, M. H. Shallow halogen vacancies in halide optoelectronic materials. *Physical Review B - Condensed Matter and Materials Physics* **2014**, *90*, 1–6.
- (71) Sebastian, M.; Peters, J. A.; Stoumpos, C. C.; Im, J.; Kostina, S. S.; Liu, Z.; Kanatzidis, M. G.; Freeman, A. J.; Wessels, B. W. Excitonic emissions and above-band-gap luminescence in the single-crystal perovskite semiconductors CsPbBr₃ and CsPbCl₃. *Physical Review B - Condensed Matter and Materials Physics* **2015**, *92*, 1–9.
- (72) Kang, J.; Wang, L. W. High Defect Tolerance in Lead Halide Perovskite CsPbBr₃. *Journal of Physical Chemistry Letters* **2017**, *8*, 489–493.

- (73) Kang, J. Effects of band edge positions on defect structure in lead halide perovskites: A case study on the Br vacancy in CsPbBr₃. *Physical Review Materials* **2020**, *4*, 1–6.
- (74) Glazer, A. M. The classification of tilted octahedra in perovskites. *Acta Crystallographica Section B Structural Crystallography and Crystal Chemistry* **1972**, *28*, 3384–3392.
- (75) Gao, R. et al. Designing Optimal Perovskite Structure for High Ionic Conduction. *Advanced Materials* **2020**, *32*, 1–9.
- (76) Mizusaki, J.; Arai, K.; Fueki, K. Ionic conduction of the perovskite-type halides. *Solid State Ionics* **1983**, *11*, 203–211.
- (77) Narayan, R. L.; Sarma, M. V.; Suryanarayana, S. V. Ionic conductivity of CsPbCl₃ and CsPbBr₃. *Journal of Materials Science Letters* **1987**, *6*, 93–94.
- (78) Zhang, L.; Zeng, Q.; Wang, K. Pressure-Induced Structural and Optical Properties of Inorganic Halide Perovskite CsPbBr₃. *Journal of Physical Chemistry Letters* **2017**, *8*, 3752–3758.
- (79) Nagaoka, Y.; Hills-Kimball, K.; Tan, R.; Li, R.; Wang, Z.; Chen, O. Nanocube Superlattices of Cesium Lead Bromide Perovskites and Pressure-Induced Phase Transformations at Atomic and Mesoscale Levels. *Advanced Materials* **2017**, *29*.
- (80) Sun, J.; Ruzsinszky, A.; Perdew, J. Strongly Constrained and Appropriately Normed Semilocal Density Functional. *Physical Review Letters* **2015**, *115*, 1–6.
- (81) Blöchl, P. E. Projector augmented-wave method. *Physical Review B* **1994**, *50*, 17953–17979.
- (82) Kresse, G.; Furthmüller, J. Efficient iterative schemes for ab initio total-energy calculations using a plane-wave basis set. *Physical Review B - Condensed Matter and Materials Physics* **1996**, *54*, 11169–11186.

- (83) Jia, F.; Kresse, G.; Franchini, C.; Liu, P.; Wang, J.; Stroppa, A.; Ren, W. Cubic and tetragonal perovskites from the random phase approximation. *Physical Review Materials* **2019**, *3*, 1–7.
- (84) Bokdam, M.; Lahnsteiner, J.; Ramberger, B.; Schäfer, T.; Kresse, G. Assessing Density Functionals Using Many Body Theory for Hybrid Perovskites. *Physical Review Letters* **2017**, *119*, 1–5.
- (85) Shahi, C. Assessment of the Meta-GGA SCAN and Self-Interaction Corrected SCAN Density Functional. Ph.D. thesis, Temple University, 2019.
- (86) Isaacs, E. B.; Wolverton, C. Performance of the strongly constrained and appropriately normed density functional for solid-state materials. *Physical Review Materials* **2018**, *2*, 1–11.
- (87) Monkhorst, H. J.; Pack, J. D. Special points for Brillouin-zone integrations. *Physical Review B* **1976**, *13*, 5188–5192.
- (88) Xue, J.; Yang, D.; Cai, B.; Xu, X.; Wang, J.; Ma, H.; Yu, X.; Yuan, G.; Zou, Y.; Song, J.; Zeng, H. Photon-Induced Reversible Phase Transition in CsPbBr₃ Perovskite. *Advanced Functional Materials* **2019**, *29*, 1–8.
- (89) De Souza, R. A.; Mueller, D. N. Electrochemical methods for determining ionic charge in solids. *Nature Materials* **2020**,
- (90) Mott, N. F.; Gurney, R. W. *Electronic Processes in Ionic Crystal*, 2nd ed.; Oxford University Press: Oxford, 1950.
- (91) Genreith-Schriever, A. R.; De Souza, R. A. Field-enhanced ion transport in solids: Reexamination with molecular dynamics simulations. *Physical Review B* **2016**, *94*, 4–8.

- (92) Salles, N.; Martin-Samos, L.; de Gironcoli, S.; Giacomazzi, L.; Valant, M.; Hemeryck, A.; Blaise, P.; Sklenard, B.; Richard, N. Collective dipole effects in ionic transport under electric fields. *Nature Communications* **2020**, *11*, 1–7.

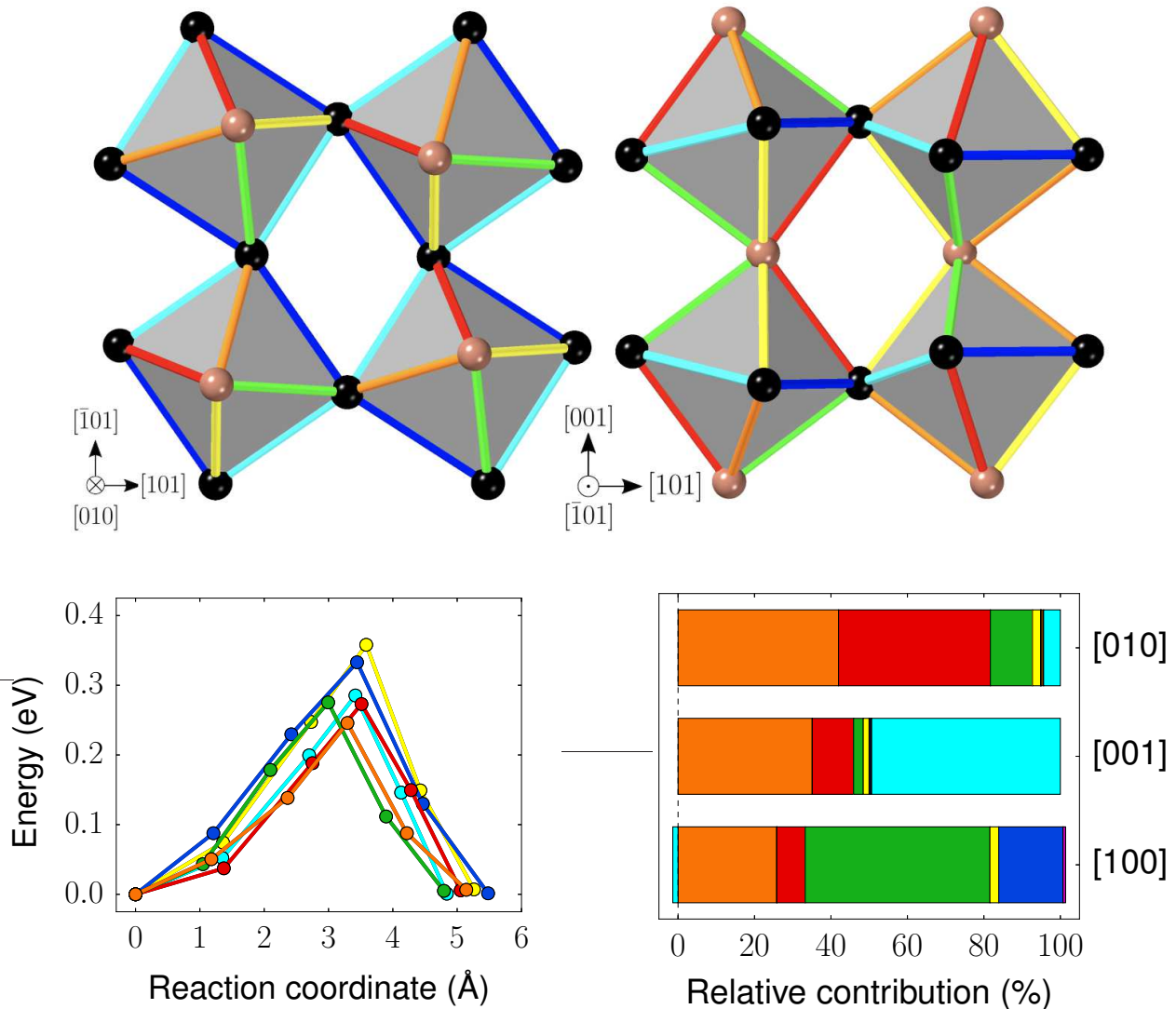


Figure 1: Top row: Structure of the $Pnma$ phase of $CsPbBr_3$ at 0.0 GPa. Only the bromide ions are shown, with the symmetrically inequivalent apical and equatorial bromide sites represented by pink and black spheres, respectively. The symmetrically inequivalent *pairs* of 1-NN bromide ions are connected along the edges of the $PbBr_3$ octahedra by colour-coded sticks. On the left, the structure is viewed along the b (long) axis, thus highlighting the connectivity in the equatorial plane, while on the right, the structure is viewed along the $[\bar{1}01]$ direction, highlighting the connectivity along the b axis, which points up the page. Bottom left; the energy barriers for positively charged bromide vacancy migration along the symmetrically inequivalent paths, at 0.0 GPa. Bottom right; the relative contributions of transitions between each symmetrically inequivalent pair to the overall mobility, at 0.0 GPa.

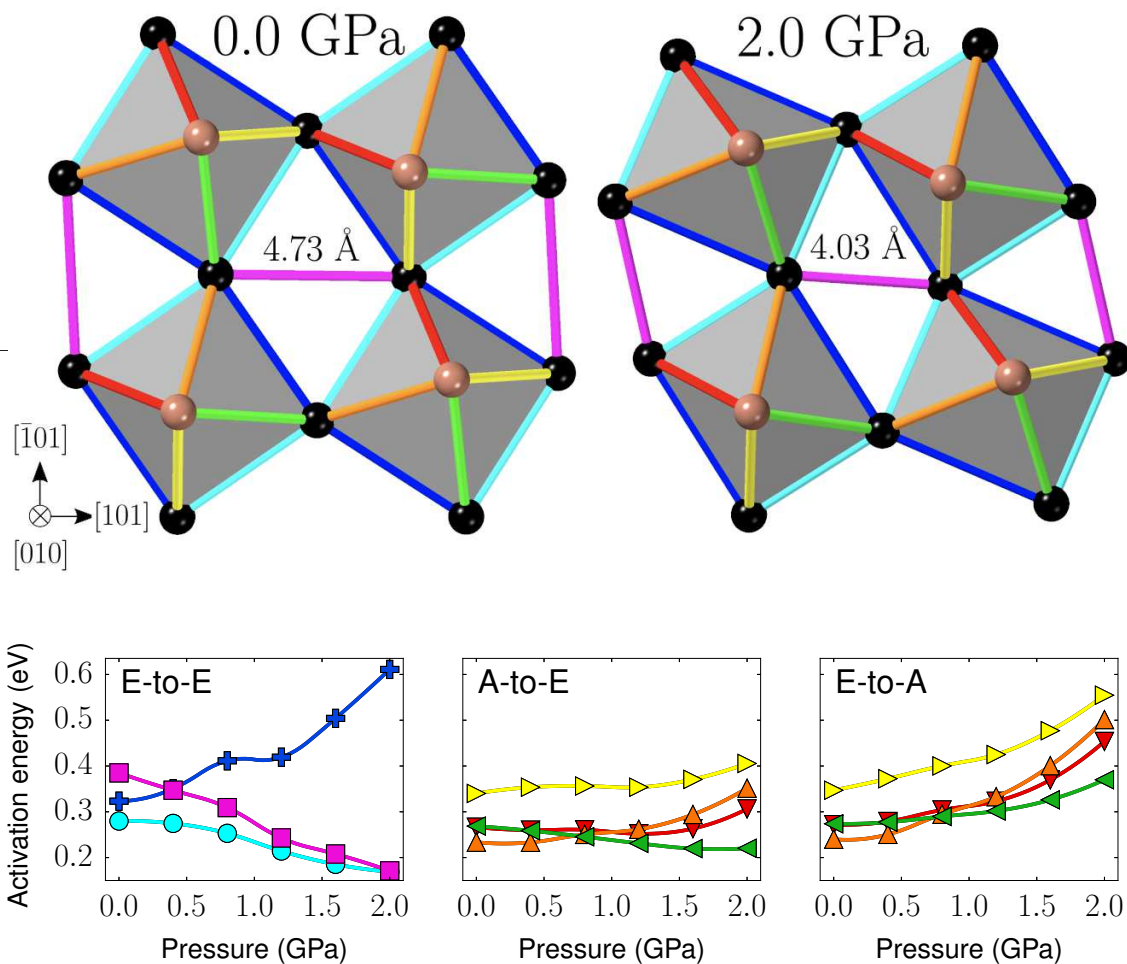


Figure 2: Top row: Visual representation of the 2-NN pair of bromide sites, connected by a magenta stick, showing the large reduction in distance between them at 2.0 GPa (right) in comparison to 0.0 GPa (left). Bottom row; the energy barriers for vacancy migration under pressure for equatorial-to-equatorial (E-to-E), apical-to-equatorial (A-to-E) and equatorial-to-apical (E-to-A) paths, respectively.

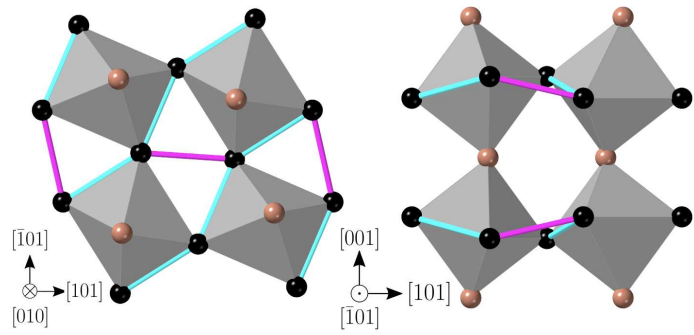
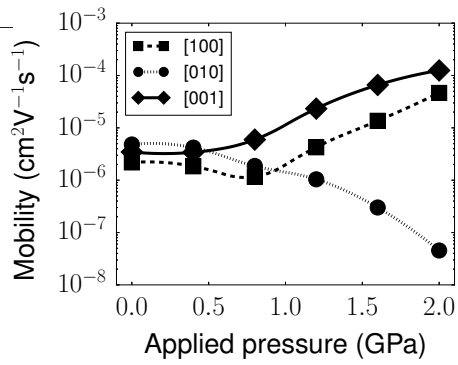


Figure 3: Left: Dependence of the diagonal components of the mobility tensor on pressure, exhibiting an effective 3D-to-2D transition as pressure is increased. Centre and right: CsPbBr₃ structure at 2.0 GPa from two different perspectives, showing the two pairs of lattice sites, the transitions between which contribute overwhelmingly to the mobility at that pressure.